Simulations and Experiments on Low-Pressure Permeation of Fabrics: Part I—3D Modeling of Unbalanced Fabric

F. D. DUNGAN, M. T. SENOGUZ, A. M. SASTRY[1] AND D. A. FAILLACI
Department of Mechanical Engineering
2140 G.G. Brown Building
2350 Hayward Street
The University of Michigan
Ann Arbor, Michigan 48109-2125

ABSTRACT: Conformation of fabrics to complex molds during composite processing induces significant fabric deformation and local shear, which in turn alter the processability of these preforms from their unsheared, flat configuration. The present work (Parts I and II) establishes that although composite mold processing can often be described generally by a percolation flow assumption (e.g., Darcy or Poiseuille flow), changes in microarchitecture of fabric in shear result in markedly different flow fronts. We reiterate our earlier finding that use of a transformed Darcy law (i.e., mathematical transformation of tensor of undeformed permeability, to the sheared configuration) does not accurately predict permeability for sheared fabrics. In essence, the effect of the change in microarchitecture of the fabric is not captured by mathematical transformation of the tensorial permeability. We also point out the deficiencies of semi-empirical approaches in determining sheared fabric permeability. We then develop a 3D fabric model, which is used to quantify the effects of nesting and changes in gap architecture with shear angle. We show that nesting produces gaps in molds in commonly-used permeability experiments which easily exceed single-layer fabric thicknesses when more than a few layers are used, but that this condition is easily detectable in an experiment (i.e., Poiseuille flow between topmost layer and mold top is easily detected). We also show that shear angle (in our case, $\theta = 0°$, 15°, and 30°) produces little difference in nesting, though it significantly alters fabric microstructure and the sizes and shapes of intralayer gaps. In Part II of this paper, we use this fabric model to predict fabric permeability. Our work suggests that departure from the more traditional approach of generation of a large suite of data from permeation experiments to determine manufacturability of preforms, in favor of computational simulation of fabric geometries, is well-justified.

[1]Author to whom correspondence should be addressed. E-mail: amsastry@umich.edu

0021-9983/01/14 1250–35 $10.00/0 DOI: 10.1106/5A3P-K6WA-FKVQ-1RF4

Journal Online at http://techpub.metapress.com

INTRODUCTION

THE RAPID ADVANCEMENT of composite processing has required constant re-evaluation of controls, transport, mechanical and rheological techniques for modeling. Processing science has advanced from its aerospace roots involving highly labor-intensive preparation of precisely aligned fibers to more modern injection schemes involving complex reinforcement architectures for civil and mechanical structural applications. Semi-empiricism has given way to greater use of computational prediction of flow fronts, temperatures and deformations during processing.

Low-pressure penetration of fabric by viscous fluid is a key phenomenon in many such processes, with the majority of fluid penetration modeling approaches stemming from Darcy's law. Use of this approach requires generation of reinforcement permeability, and previous work has resulted in a large number of studies on particular fabrics, and even some large databases of permeabilities. Published permeabilities from different groups for similar process conditions, however, show substantial disagreement. Calhoun et al. (1996), for example, documented experiments on the same 8-harness carbon fabric, Celion G105 (G30-500), by several research groups which yielded results with an order of magnitude difference in permeability.

The disagreement in the literature on rather simple bench-scale experiments, the failure of the empirical approach to produce good predictions of flow front location in complex parts without extensive "correction" of permeabilities, and thus the high intrinsic cost of the approach, motivate this study. Some simplification in the modeling of viscous fluid penetration in reinforcement materials is required at the present time because of the practical barriers in solving the full Navier-Stokes equations in complex domains. These include both computation time and singularities generated by boundaries. Moreover, many practical processes, including resin transfer molding, employ sufficiently low pressures and resin viscosities that approximation of the flow by a creeping flow assumption, wherein pressure gradient is linearly proportional to flow front velocity (e.g., Darcy's law or Poiseuille flow) is valid. The Darcy-type flow may be described (in 2D, accounting for material anisotropy) as

$$\bar{v} = \frac{-1}{\mu}\begin{bmatrix} K_{11} & K_{12} \\ K_{12} & K_{22} \end{bmatrix}\nabla P \tag{1}$$

where $\bar{v}$ is the average fluid velocity, μ the fluid viscosity, K the permeability of the porous medium, and ∇P the pressure gradient.

Previously (Dungan et al., 1999), we investigated the use of the unsheared permeabilities in a transformation described in Dungan (2000) to evaluate whether the unsheared values alone could be used to generate permeabilities for

sheared fabric, thereby avoiding the experimental determination of permeabilities for a wide range of shear angles. Since plain-weave fabrics are commonly-used reinforcements for textile composites (e.g., Tan et al., 1997), we considered unbalanced plain woven Knytex 24-5×4, with material geometry shown in Figure 1 and properties given in Table 1. Fabric properties were obtained from the manufacturer or calculated from the manufacturer's data, except for the lock angle, which was measured in our laboratory. The viscosities of the impregnating fluids given in Table 1 were measured using a Ferranti-Shirley viscometer equipped with parallel disks. Reynolds numbers were less than $1.5 * 10^{-2}$. The formulation given in Tucker and Dessenberger (1994) was used to obtain Re as

$$\mathrm{Re} = \frac{\rho V \sqrt{K}}{\mu} \tag{2}$$

Figures 2(a) and 2(b) give schematics of the fabric geometry and experimental setup (Dungan et al., 1999). The asymmetry of an unbalanced fabric allowed investigation of the relative importance of capillarity and gaps between tows. The experimental study uncovered significant discrepancy in both actual values and trends in permeability for sheared/unsheared configuration using a tensor transformation of the permeabilities in the unsheared configuration, as shown in Figures 3(a) and 3(b), as well as Table 2. In these figures, we add to the analysis of Dungan et al. (1999) a correction for volume fraction, via use of a Kozeny-Carman approach (Smith et al., 1997), as

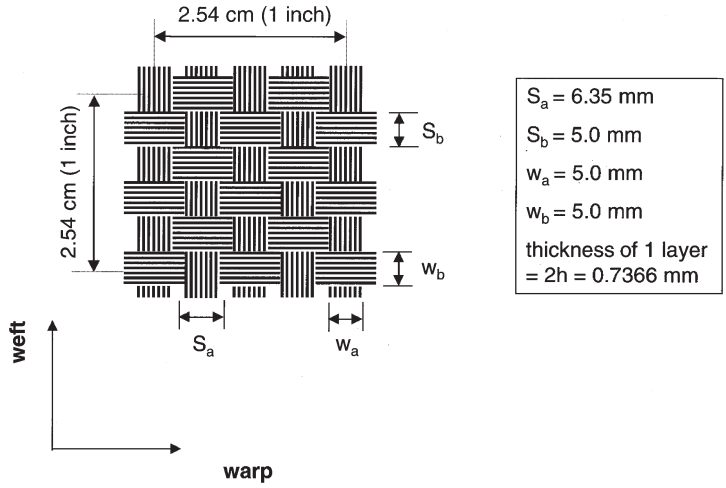

Figure 1. *Structure of Knytex 24-5×4.*

Table 1. Material properties for Knytex 24-5×4 and corn oil, both clear and dyed.

Knytex 24-5×4 Plain-Weave Fabric	
Fiber composition	E-glass
Density of fiber material	2590 kg/m^3 (0.0935 lb/in^3)
Linear density of tows	207 yd/lb
Volume fraction of one layer of fabric	45.4%
Warp intratow volume fraction	78.6%
Weft intratow volume fraction	78.2%
Numbers of warp tows per inch	5
Numbers of weft tows per inch	4
Width of warp tows	5 mm
Width of weft tows	5 mm
Thickness of one layer of fabric	0.7366 mm
Number of glass fibrils per warp tow	4020
Number of glass fibrils per weft tow	4020
Diameter of a fibril	17.2 μm
Fabric lock angle	33 degrees
Clear Corn Oil	
Density	893 kg/m^3
Viscosity	0.040 kg/(m·s)
Dyed Corn Oil	
Density	892 kg/m^3
Viscosity	0.044 kg/(m·s)

$$K = \frac{R^2}{4c}\frac{(1 - V_f)^3}{V_f^2} \tag{3}$$

where c is the Kozeny constant ("dependent on the geometric form of the bed") and R is the fiber diameter. Since R and c are constant for a given fabric, the permeabilities calculated using the tensor transformation described in Dungan (2000) were corrected using the equation

$$K(\theta)_{corrected} = \left(K_{0,uncorrected} \frac{(V_{f_0})^2}{(1 - V_{f_0})^3} \right) \frac{(1 - V_f(\theta))^3}{(V_f(\theta))^2} \tag{4}$$

where subscript 0 refers to the unsheared state, and volume fraction varies according to

$$V_f(\theta) = \frac{V_{f_0}}{\sin(90 - \theta)} \tag{5}$$

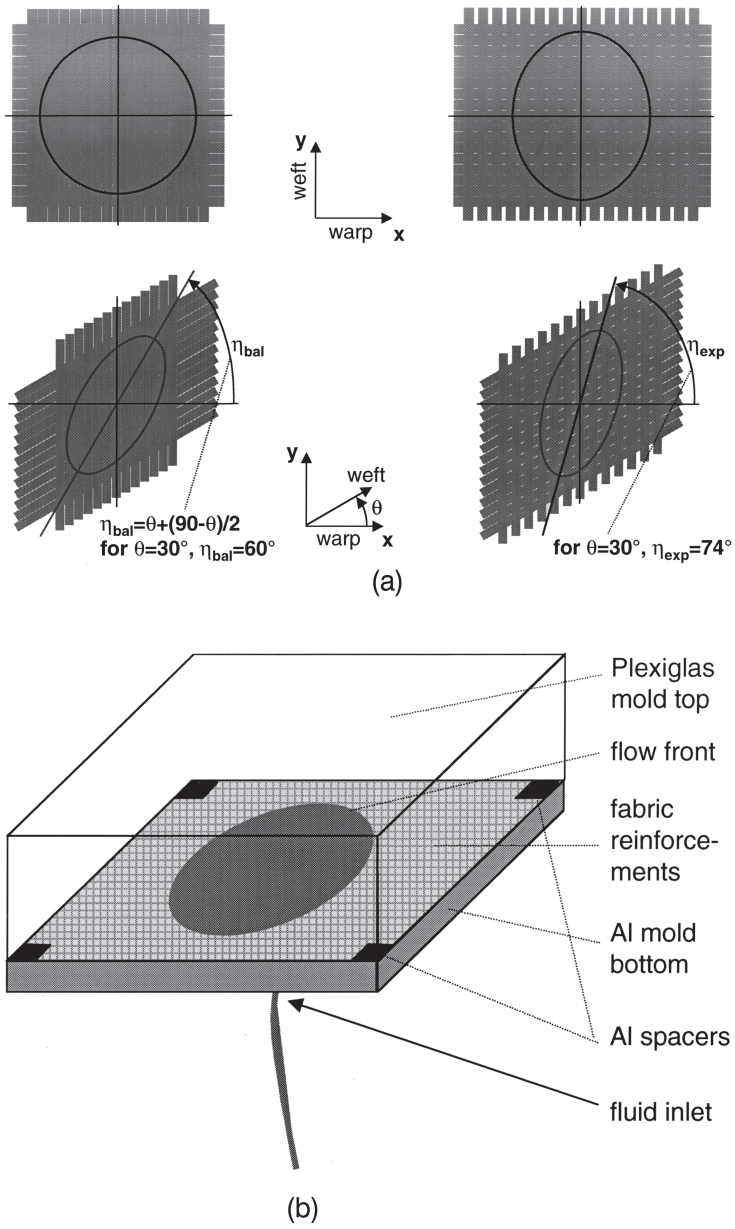

Figure 2. *Experimental approach: (a) Schematics of flow front shapes and orientations for balanced fabric (left) and observed for unbalanced Knytex 24-5×4 (right). Typical flow front shapes and orientations are shown for unsheared (top) and sheared (bottom) fabric, (b) flow injection through mold bottom.*

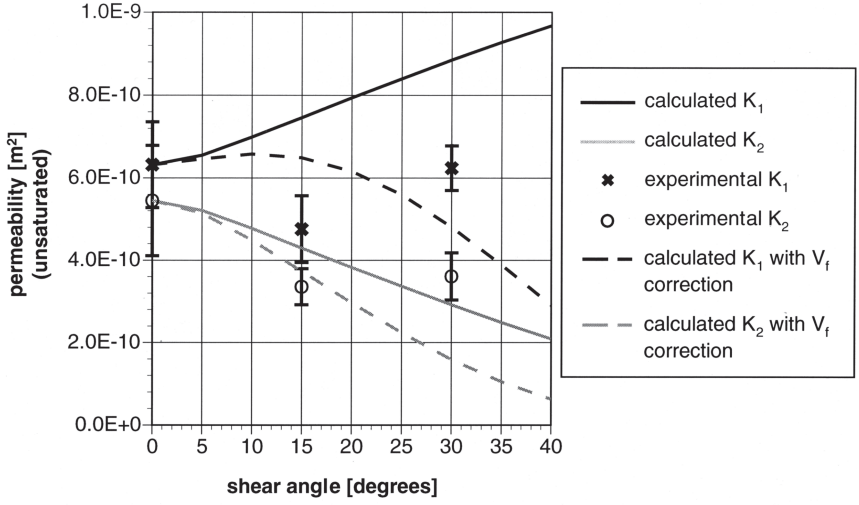

(a)

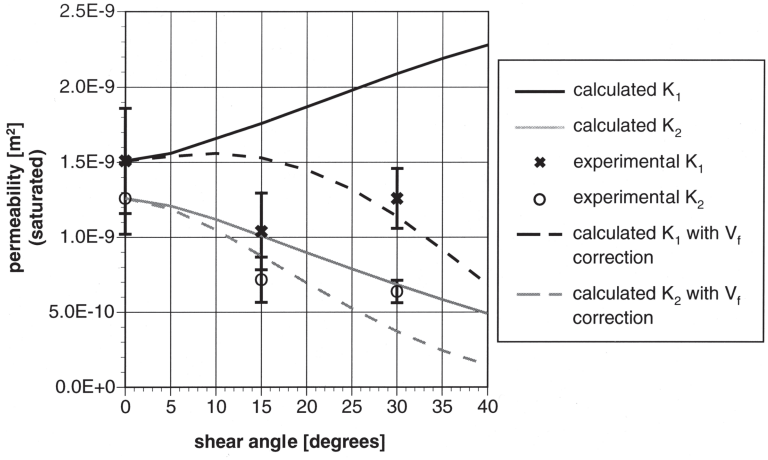

(b)

Figure 3. *Experimentally determined permeabilities and tensor-transformed permeabilities obtained from unsheared configuration, for (a) unsaturated flow and (b) saturated flow. The error bars on the experimental data represent ±σ, i.e., a confidence of 68.26% for a normal distribution.*

Table 2. Principal permeabilities for Knytex 24-5×4 obtained from experiment (Dungan et al., 1999).

Unsaturated Flow				
Shear Angle (degrees)	**Average Experimental K_1 (m^2)**	**K_1 Based on Transformed Unsheared K's with V_f Correction (m^2)**	**Average Experimental K_2 (m^2)**	**K_2 Based on Transformed Unsheared K's with V_f Correction (m^2)**
0	$6.32 * 10^{-10}$	$6.23 * 10^{-10}$	$5.45 * 10^{-10}$	$5.45 * 10^{-10}$
15	$4.76 * 10^{-10}$	$6.49 * 10^{-10}$	$3.36 * 10^{-10}$	$3.74 * 10^{-10}$
30	$6.24 * 10^{-10}$	$4.81 * 10^{-10}$	$3.61 * 10^{-10}$	$1.59 * 10^{-10}$
Saturated Flow				
Shear Angle (degrees)	**Average Experimental K_1 (m^2)**	**K_1 Based on Transformed Unsheared K's with V_f Correction (m^2)**	**Average Experimental K_2 (m^2)**	**K_2 Based on Transformed Unsheared K's with V_f Correction (m^2)**
0	$1.51 * 10^{-9}$	$1.51 * 10^{-9}$	$1.26 * 10^{-9}$	$1.26 * 10^{-9}$
15	$1.04 * 10^{-9}$	$1.53 * 10^{-9}$	$7.17 * 10^{-10}$	$8.76 * 10^{-10}$
30	$1.26 * 10^{-9}$	$1.14 * 10^{-9}$	$6.38 * 10^{-10}$	$3.72 * 10^{-10}$

Even with the volume fraction correction, use of unsheared permeability to model the permeability in sheared configurations produces poor agreement.

Note that an expression of the form

$$V_f(\theta) = \frac{V_{f,\max} V_f}{V^{uc} V_{f,\max} \sin(90 - \theta) + V_f \sin(\theta)} \tag{6}$$

could be used to eliminate the nonphysical infinite result for volume fraction at 90 degrees (and producing the maximum volume fraction for a particular packing scheme); however, differences between the two expressions are rather small for angles less than a typical fabric lock angle.

Data from Dungan et al. (1999) were combined with additional experimental data from the present study for 15 degrees of shear. Comparisons were further expanded to include comparisons of permeability ratios and principal flow directions with a semi-empirical model (Lai and Young, 1997, 1999). Our notation is given in Figure 4. θ is the fabric shear angle, η is the principal flow direction angle, x and y are the fixed coordinate axes, a and b are the directions aligned with the warp and weft, respectively. Shear is applied via rotation of the warp tows coun-

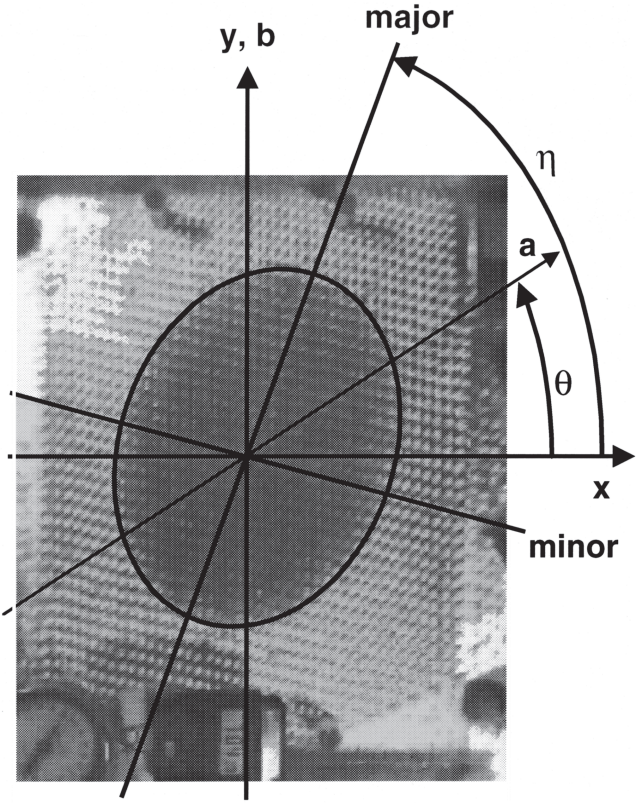

Figure 4. *Coordinate system for the present work.*

ter-clockwise from their original position parallel to the *x* axis; weft tows are held parallel to the *y* axis. Comparisons between our data (corrected for an angle transformation error in Dungan et al., 1999) and the semi-empirical approach of Lai and Young (1997) are shown as Figures 5 and 6, for principal flow angle and ratio of principal permeabilities, respectively. There is a relatively weak correspondence of the empirical curves to the data, with no single parameter fitting all three shear angles tested. It is important to note that the technique investigated for use with our data (Lai and Young, 1997, 1999) only allowed prediction of the ratio of principal permeabilities and the flow front orientation angle; actual permeabilities in the unsheared configuration are inputs to the empirical model.

Here, we focus on development and validation of a more robust technique for determining the effect of local architecture on fluid front penetration, including prediction of values of principal permeabilities (without resort to initial experi-

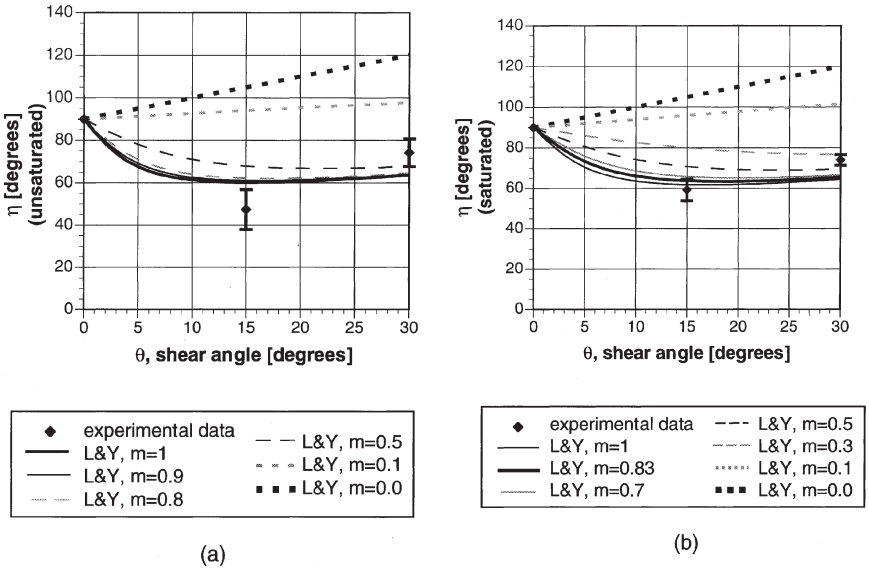

Figure 5. *Comparison of experimentally determined principal flow directions with semi-empirical approach of Lai and Young (1997), for (a) unsaturated and (b) saturated conditions, in notation of the present work.*

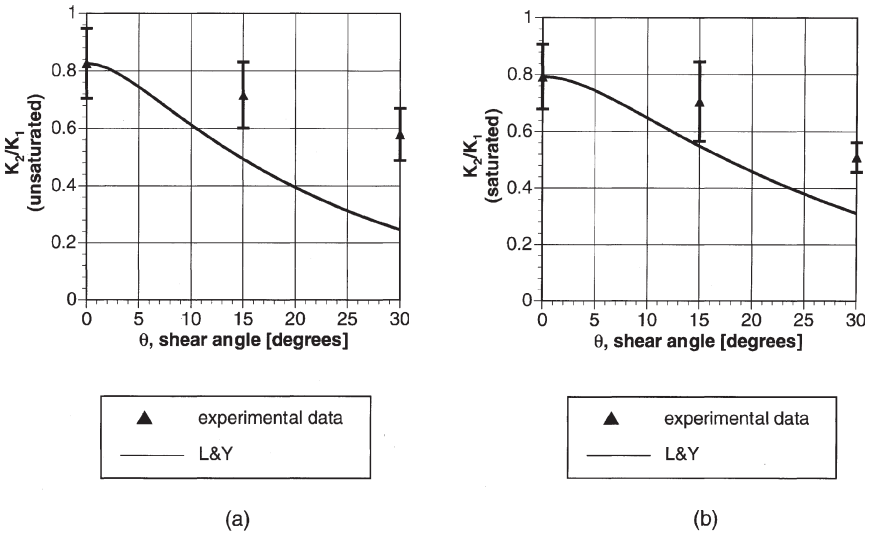

Figure 6. *Comparison of ratio of experimentally determined permeabilities with semi-empirical approach of Lai and Young (1997), for (a) unsaturated and (b) saturated conditions.*

ments) and flow front orientations. Three main hypotheses motivate the present study:

1. Low-pressure, viscous fluid penetration of fabrics is linear (i.e., can be described by a constitutive equation linearly relating pressure gradient and velocity, such as Darcy's Law or Poiseuille flow).
2. Fluid penetration in these cases is predominantly determined by gap architecture, so that capillarity and other surface effects do not significantly affect flow in practical processes.
3. Gap architecture changes significantly in the presence of fabric shear, resulting in calculable critical gap dimensions, which can be used to directly determine fabric permeability without resort to experimentation on the fabric.

The first two of these hypotheses are supported by work described in Part II of this work (Senoguz et al., 2001), wherein detailed numerical simulations are performed to establish flow behavior, using experimental geometries and material properties (Dungan et al., 1999). To validate the third hypothesis, a detailed, 3D fabric model is developed to characterize differences in fabric geometry due to shear and nesting of layers.

DEVELOPMENT OF A 3D FABRIC MODEL

Previous Work

Various shapes of tow cross-sections in fabrics have been assumed, as shown schematically in Figure 7, with relevant parameters for some of these models shown in Figure 8. A brief synopsis of major approaches follows:

1. Rectangular cross-sections (Binétruy et al., 1998), shown in Figure 7(a), where spaces between fibers inside tows were designated "micropores," and open regions between tows were designated "macropores."
2. Elliptical cross-sections (Phelan and Wise, 1996), shown in Figure 7(b).
3. Circular cross-sections (Peirce, 1937), where the yarn was assumed to be straight except where wrapped around the crossing thread. Descriptive parameters [Figures 7(c) and 8(a)] included yarn length, l, crimp height, h, thread spacing, p, and sum of diameters of two yarns, D, related as:

$$p = (1 - D\theta)\cos\theta + D\sin\theta \tag{7}$$

$$h = (1 - D\theta)\sin\theta + D(1 - \cos\theta) \tag{8}$$

$$h_1 + h_2 = D \tag{9}$$

4. Sections comprised of intersecting circular arcs (Dasgupta and Agarwal, 1992).

Parameters [Figures 7(d) and 8(b)] included the radius of the arc defining the cross-section ρ, arc length s, and radius of yarn undulation l, related as

$$\rho = \frac{c^2 + a^2}{2a} \tag{10}$$

$$s = l\cos^{-1}\left[\frac{1-(a+0.5b)}{1}\right] \tag{11}$$

$$l = \frac{(c+d)^2 + (a+0.5b)^2}{2(a+0.5b)} \tag{12}$$

5. Unit cell geometry defined as the interior region bounded by 4 sinusoidal curves (McBride and Chen, 1997). Parameters included yarn thickness h, length of unit-cell base or distance between interlacing points S, width of the yarn (normalized by sine of the yarn angle) w, and the half-period of $y_3(x)\beta$, related as:

$$y_1(x) = \frac{h}{2}\left[\cos\frac{\pi x}{S} + 1\right] \qquad (0 < x < S) \tag{13}$$

$$y_2(x) = \frac{h}{2}\left[\cos\frac{\pi x}{S} - 1\right] \qquad (0 < x < S) \tag{14}$$

$$y_3(x) = -h\cos\left[\frac{\pi x}{\beta}\right] \qquad \left(0 < x < \frac{w}{2}\right) \tag{15}$$

$$y_4(x) = -h\cos\left[\frac{\pi(x-(S-\beta))}{\beta}\right] \qquad \left(S - \frac{w}{2} < x < S\right) \tag{16}$$

Because of the good agreement shown by McBride and Chen (1997) between fabric response and modeling, the basic tow cross-sectional representation shown in Figure 7(e) was adopted here, with some extension, as shown in Figures 7(f) and 8(c).

Definition of a Fabric Representative Cell

The model by McBride and Chen (1997) was first generalized to allow analysis of unbalanced fabrics. Also, despite the complete description of an individual 2D

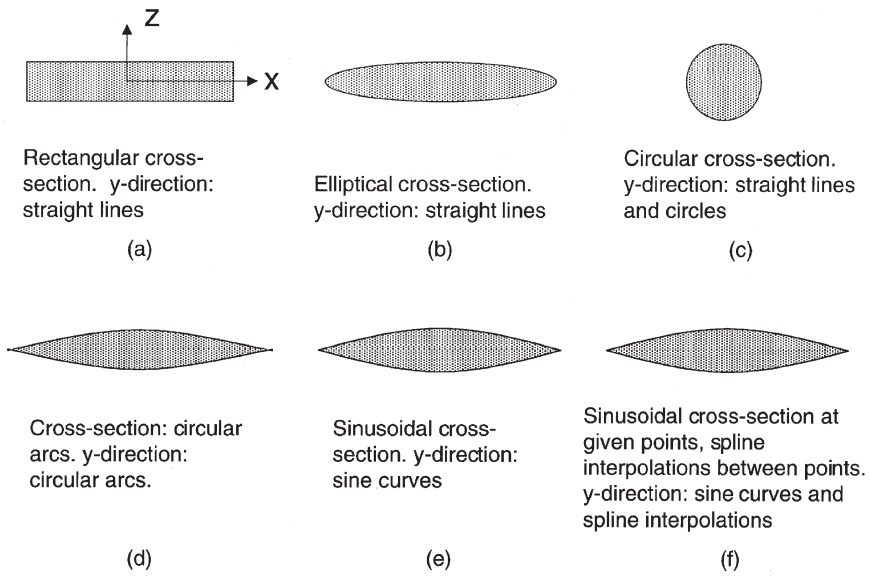

Figure 7. *Possible tow representations. Axes are shown in (a). Representations include (a) Binétry et al. (1998), (b) Phelan and Wise (1996), (c) Peirce (1937), (d) Dasgupta and Agarwal (1992), (e) McBride and Chen (1997) and (f) present approach.*

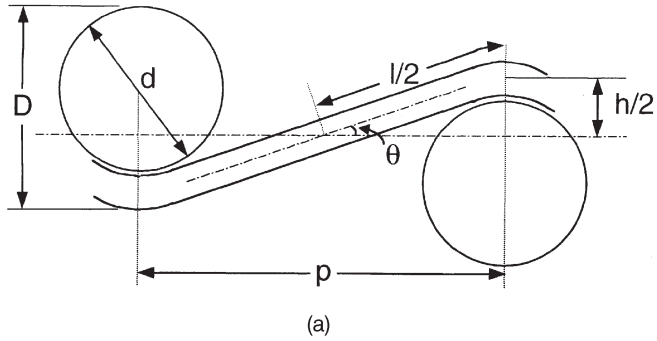

Figure 8. *Geometric parameters for three models: (a) Peirce (1937), (b) Dasgupta and Agarwal (1992), and (c) our model, where functions defined in the* a *and* b *directions are shown on the left and right, respectively. Other edges are translations and/or rotations of the functions shown.*

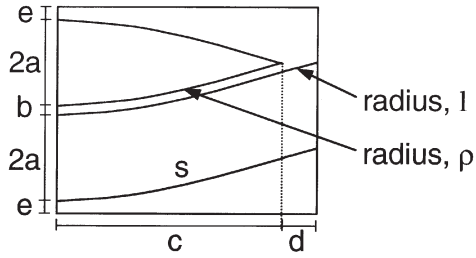

(b)

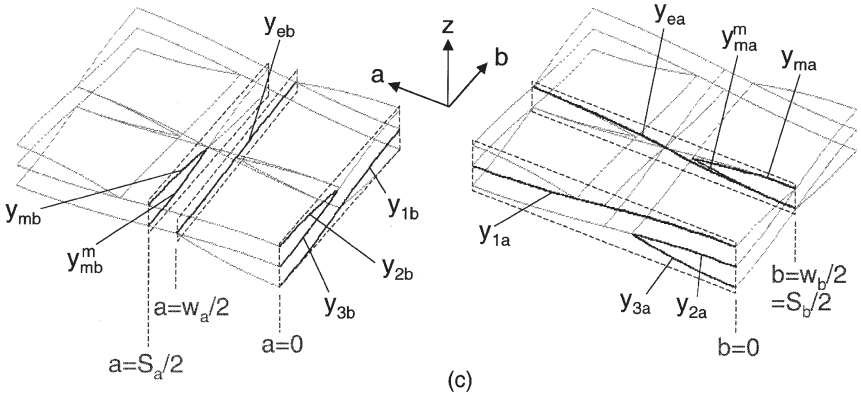

(c)

Figure 8 (continued). *Geometric parameters for three models: (a) Peirce (1937), (b) Dasgupta and Agarwal (1992), and (c) our model, where functions defined in the* a *and* b *directions are shown on the left and right, respectively. Other edges are translations and/or rotations of the functions shown.*

transverse fabric section, an assumption for tow geometry was required in order to make the model fully three-dimensional.

The model of McBride and Chen (1997) called for extrusion of the defined fabric cross-section along a sine curve, out-of-plane, to create a full tow. However, this description is only feasible in the case of a symmetric cross-section. For the general case, the cross-section is antisymmetric, since the shapes of a tow cross-section at both ends of a symmetric representative cell are reflections of each other with respect to the *x*-*y* plane, as shown in Figure 9(a).

In order to make the model fully three-dimensional, we defined the cross-section in the middle of the symmetric representative cell as symmetric. We also defined an additional sine curve to connect the sharp corners of the half-tows at both ends of the representative cell and in the middle of the symmetric representative cell. We denote a piece of fabric containing exactly two half-tows of both the warp and the weft as the "symmetric representative cell." A fully "representative" cell may be constructed by combining two or more pieces that span a full tow in both the warp and the weft. Such cells, while containing enough geometric information to fully define the fabric in terms of location of gaps and tows, are not denoted "symmetric."

Figure 9(b) shows a representative cell of thickness 2*h* with its dimensions in the *x*-*y* plane. Cross-sections at the midpoints of the representative cell were defined through enforcement of symmetry; tows were created with spline surfaces between curves. A fully 3D representation (as opposed to a series of cross-sections at particular points, e.g., crossover points) resulted from appropriate reflections and translations of a single cell. In the expressions that follow, the subscript 0 denotes a value in the unsheared configuration, and 90°-θ represents the angle between the warp and the weft. Coordinates a and b denote the directions parallel to the warp and weft, respectively, as shown in Figure 9(c).

The upper boundary of the cross-section of half of a weft tow is given by

$$y_{2a}(x) = \frac{h}{2}\cos\left(\left(\frac{\pi x}{S_a}\right) - 1\right) \qquad 0 < x < \frac{w_a(\theta)}{2} \tag{17}$$

at the edges of the symmetric representative cell and

$$y_{ma}(x) = \frac{h}{2}\left(\cos\left(\frac{\pi x}{w_a(\theta)}\right) + 1\right) \qquad 0 < x < \frac{w_a(\theta)}{2} \tag{18}$$

at the midplane of the symmetric representative cell.

The lower boundary of the cross-section of half of a weft tow is given by

$$y_{3a}(x) = -h\cos\left(\frac{\pi x}{\beta_a(\theta)}\right) \qquad 0 < x < \frac{w_a(\theta)}{2} \tag{19}$$

at the edges of the symmetric representative cell and

$$y^m_{ma}(x) = -\frac{h}{2}\left(\cos\left(\frac{\pi x}{w_a(\theta)}\right) - 1\right) \qquad 0 < x < \frac{w_a(\theta)}{2} \tag{20}$$

at the midplane of the symmetric representative cell. The geometric function $w_a(\theta)$ is given by

$$w_a(\theta) = \frac{w_{a0}}{(\sin(90-\theta))^{(S_a - w_{a0})/\beta_{a0}}} \tag{21}$$

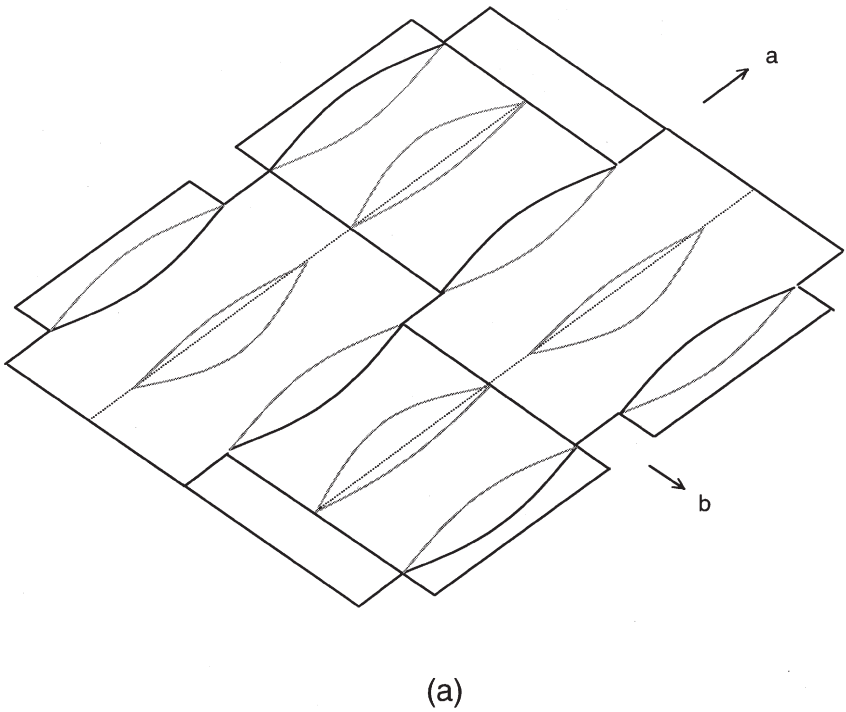

(a)

Figure 9. *Fabric microstructure, with (a) axisymmetry of tows shown here for weft tows, (b) top view of sheared fabric showing a representative cell, and (c) top view of a piece of fabric in unsheared (left) and sheared (right) configurations, showing* a *and* b*, the directions aligned with the warp and weft, respectively.*

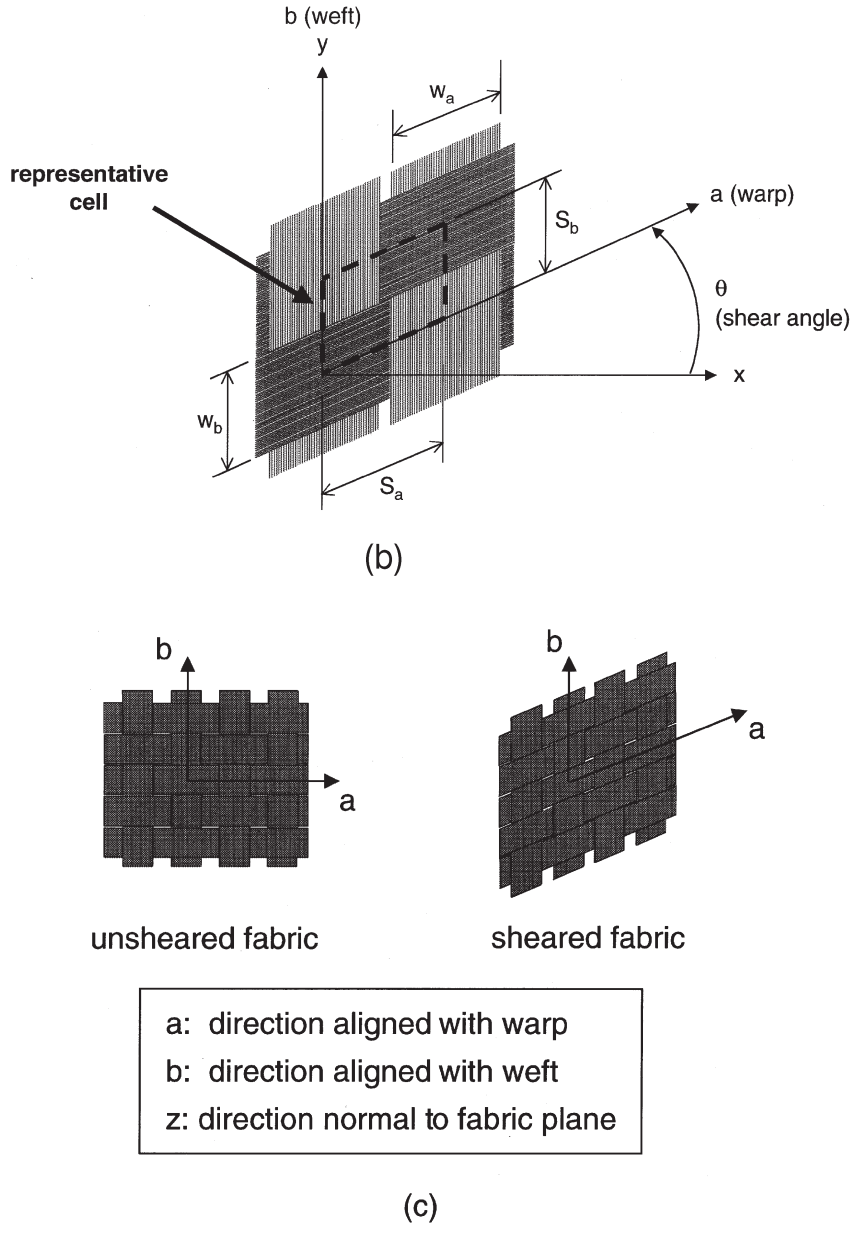

Figure 9 (continued). *Fabric microstructure, with (a) axisymmetry of tows shown here for weft tows, (b) top view of sheared fabric showing a representative cell, and (c) top view of a piece of fabric in unsheared (left) and sheared (right) configurations, showing* a *and* b*, the directions aligned with the warp and weft, respectively.*

and the function β_a is defined as

$$\beta_a(\theta) = \frac{\pi w_a(\theta)}{2\cos^{-1}\left(\sin^2\left(\frac{\pi w_a(\theta)}{4S_a}\right)\right)} \tag{22}$$

The upper boundary of the cross-section of half of a warp tow is given by

$$y_{2b}(y) = \frac{h}{2}\left(\cos\left(\frac{\pi y}{S_b}\right) - 1\right) \qquad 0 < y < \frac{w_b(\theta)}{2} \tag{23}$$

at the edges of the symmetric representative cell and

$$y_{mb}(y) = \frac{h}{2}\left(\cos\left(\frac{\pi y}{w_b(\theta)}\right) - 1\right) \qquad 0 < y < \frac{w_b(\theta)}{2} \tag{24}$$

at the midplane of the symmetric representative cell; the function $w_b(\theta)$ is defined as

$$w_b(\theta) = \frac{w_{b0}}{(\sin(90 - \theta))^{(S_b - w_{b0})/\beta_{b0}}} \tag{25}$$

The lower boundary of the cross-section of half of a warp tow is given by

$$y_{3b}(y) = -h\cos\left(\frac{\pi y}{\beta_b(\theta)}\right) \qquad 0 < y < \frac{w_b(\theta)}{2} \tag{26}$$

at the edges of the symmetric representative cell and

$$y^m_{mb}(y) = -\frac{h}{2}\left(\cos\left(\frac{\pi y}{w_b(\theta)}\right) - 1\right) \qquad 0 < y < \frac{w_b(\theta)}{2} \tag{27}$$

at the midplane of the symmetric representative cell.

β_b is a geometric parameter defined as

$$\beta_b(\theta) = \frac{\pi w_b(\theta)}{2\cos^{-1}\left(\sin^2\left(\frac{\pi w_b(\theta)}{4S_b}\right)\right)} \tag{28}$$

Between the prescribed half tow cross-sections, the shape of the tows is defined by

sinusoidal curves that connect the corners of the half tow cross-sections.

For the warp direction, the sinusoidal tow boundary function is

$$y_{ea}(x) = \frac{h}{2}\left(\cos\left(\frac{\pi w_b(\theta)}{2S_b}\right) - 1\right)\cos\left(\frac{\pi x}{S_a}\right)$$

$$-\frac{h}{2}\left(\cos\left(\frac{\pi w_b(\theta)}{2S_b}\right) - 1\right) \qquad 0 < x < S_a \tag{29}$$

for the sharp corners and

$$y_{1a}(x) = \frac{h}{2}\left(\cos\left(\frac{\pi x}{S_a}\right) + 1\right) \qquad 0 < x < S_a \tag{30}$$

for the other corners.

For the weft direction, the analogous function is

$$y_{eb}(y) = \frac{h}{2}\left(\cos\left(\frac{\pi w_a(\theta)}{2S_a}\right) - 1\right)\cos\left(\frac{\pi y}{S_b}\right)$$

$$-\frac{h}{2}\left(\cos\left(\frac{\pi w_a(\theta)}{2S_a}\right) - 1\right) \qquad 0 < y < S_b \tag{31}$$

for the sharp corners and

$$y_{1b}(y) = \frac{h}{2}\left(\cos\left(\frac{\pi y}{S_b}\right) + 1\right) \qquad 0 < y < S_b \tag{32}$$

for the other corners.

The edges were copied, reflected, and rotated as needed to create a complete representative cell, an example of which is shown in Figure 10. Tow surfaces were generated using non-uniform rational B-splines (using HYPERMESH v2.1 and v3.1) connecting appropriate sets of surface edges.

Generation of Fabric Cross-Sections

An algorithm was developed to automatically generate 2D cross-sectional descriptions of the exact fabric microstructure (tows versus gaps) at any transverse section to the plane of the fabric, at any angle to warp or weft tows. The automated approach begins with entry of section parameters into input files to HYPERMESH

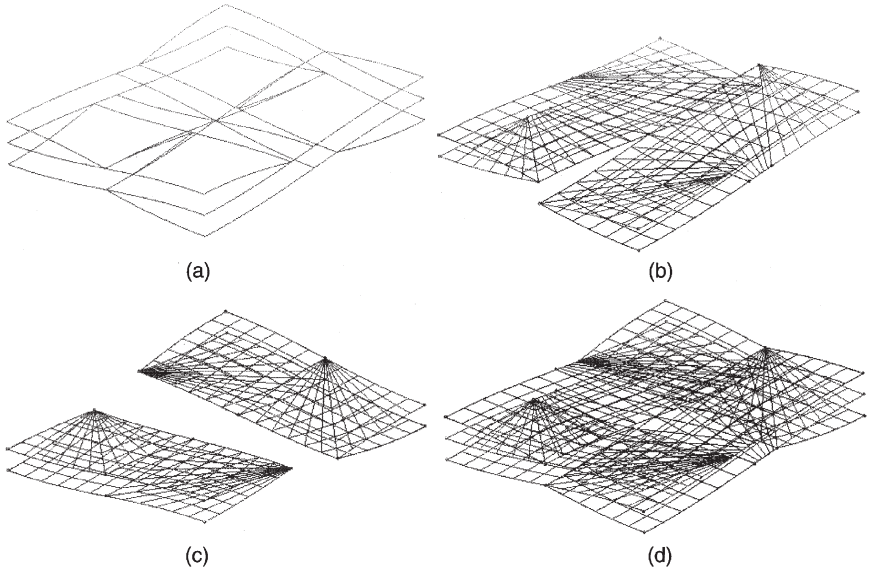

Figure 10. *Fabric model: one representative cell, with (a) edges created as sine curves, (b) warp surfaces only, (c) weft surfaces only, (d) all surfaces.*

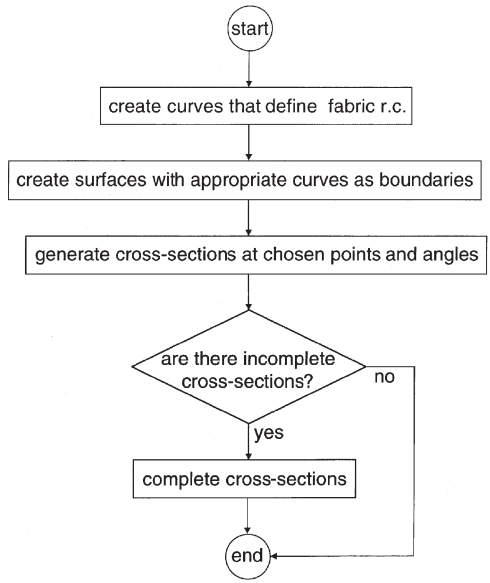

Figure 11. *Main steps required in application of the fabric model.*

as shown in the flowchart of Figure 11. Details of each step are given in Dungan (2000). Each representative cell is defined by a reference point through which the cross-section has to pass and a plane defined by angle χ, CCW from the x axis (Figure 12). The reference point is converted to an equivalent reference point on the x axis, called x_{inter}, which is defined as the intersection of the x axis with the defining plane, except if the defining plane is parallel to the x axis, in which case the reference point x_{inter} is taken as the y coordinate of the reference point.

Fabric layer thicknesses were taken to be constant, with value $2h$. The length L_{sect} of all cross-sections taken in the direction of the warp was S_a and that of all cross-sections taken in the direction of the weft was S_b. An example is shown in Figure 13, where the cross-section angle χ is 0 and all cross-sections have length $L_{sect} = S_a$.

"COMPLETING" CROSS-SECTIONS

We defined a complete cross-section as a cross-section with sufficient length to span the entire width of either both warp half-tows or both weft half-tows, whichever was shorter. For any combination of shear and cross-section angles, there is a range of X_{inter} within which cross-sections are complete, as shown in Figure 14. The range-limited case occurs when the desired cross-section spans opposite corners of the representative cell (in a top view). In this case, the cross-section goes

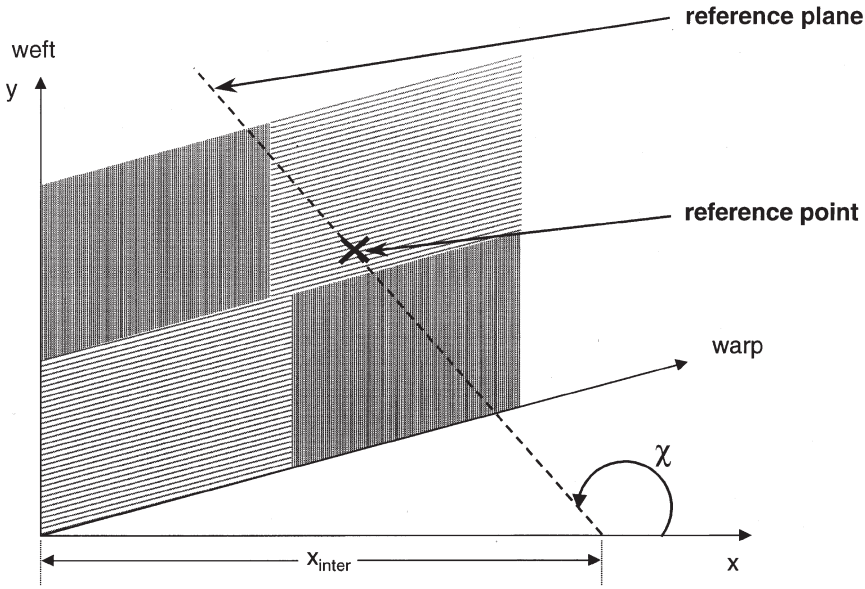

Figure 12. *Top view of a sheared representative cell with definition of a desired cross-section shown.*

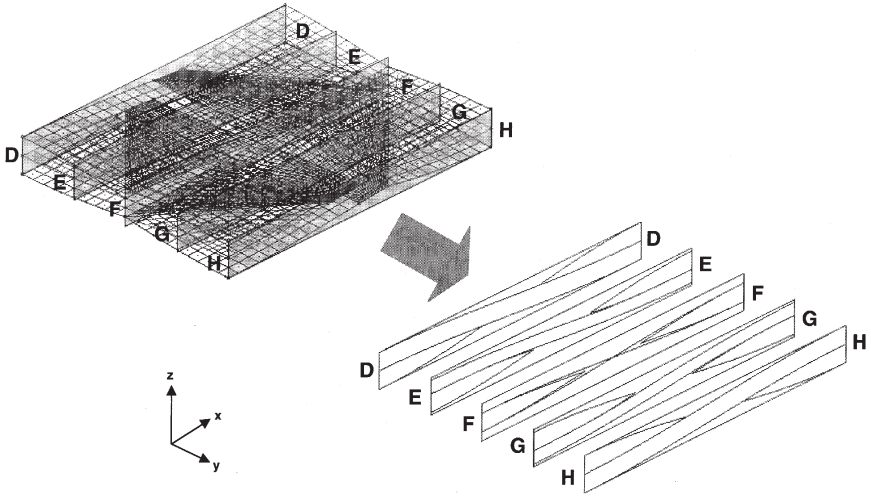

Figure 13. *Cross-sections obtained from the 3-D model. In this example, the representative cell is unsheared and the 5 cross-sections (DD, EE, FF, GG, and HH) are equidistant. The 5 cross-sections are complete since they are taken along the warp (χ = 0).*

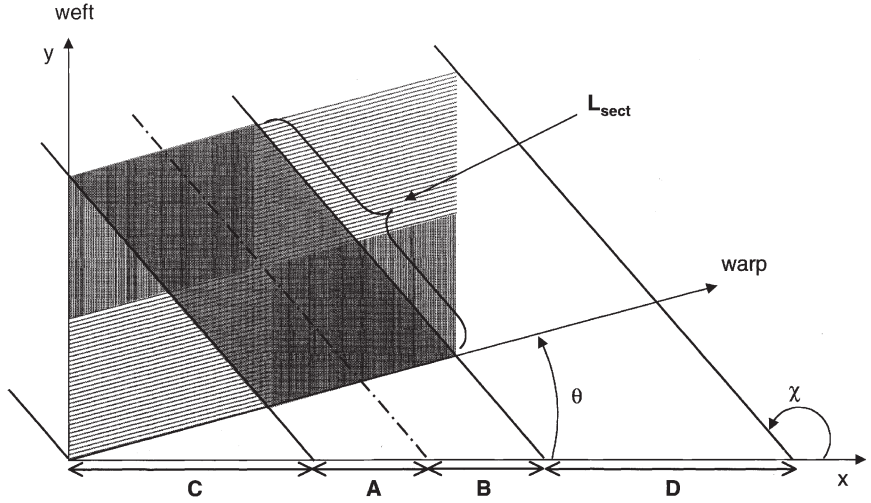

Figure 14. *Cross-sections at an arbitrary angle χ. Cross-sections in ranges A and B are complete; cross-sections in ranges C and D are incomplete and can be combined to obtain complete cross-sections. The length of complete and completed cross-sections is* L_{sect}.

through the entire width of both warp half-tows and both weft half-tows, and the range of X_{inter} within which cross-sections are complete degenerates to a point. All complete cross-sections for a given combination of θ and χ have the same length, L_{sect}, as given in Table 3. On both sides of the range of complete cross-sections is a range of incomplete cross-sections whose lengths range from L_{sect} (not included) to zero.

Figure 15 shows the parameters involved in the completion process. Cross-section 1 in Figure 15 is clearly incomplete; it can also be seen that complete cross-sections for that particular shear angle and cross-section angle include two warp half-tows. Note that any line segment along χ that includes two full weft half-tows necessarily includes more than two warp half-tows in the example. Cross-section 2 completes cross-section 1; however, cross-section 2 is in a different representative cell (shown in a lighter shade). To minimize calculation, only a single representative cell was used for any combination of shear and fabric angles. A neighboring representative cell sharing an edge with the original can be obtained by reflecting the original cell with respect to the x axis, the y axis, and the z axis. Thus, in Figure 15, cross-sections 2 and 4 are the same, and cross-section 3 can be obtained from cross-section 4 by a 180 degree rotation about the z axis. Cross-section 1 is completed using cross-section 3 or 4 with appropriate reflections and translations (and rotation, in the case of cross-section 3).

The same completion technique can be applied to any other incomplete cross-section in the representative cell. The complete and completed cross-sections for a given shear angle θ and cross-section angle χ have the same overall dimensions, with length L_{sect}, calculated using the formulae contained in Table 3. Examples of complete and completed cross-sections are given in Figure 16.

Angles α_1 and α_2 are defined as the angles between the x axis and the major and minor diagonals of the representative cell, respectively, as shown in Figure 17. They are given by

Table 3. Four cases examined for completion of cross-sections by reflection, rotation, and translation of unit geometry.

Case Designation	Range of χ	Half-Tows Full Cross-Sections Go Through	Length of Completed Cross-Section
1	$0 \le \chi \le \alpha_1$	warp	$\frac{s_a \cos\theta}{\cos\chi}$
2	$\alpha_1 \le \chi \le 90°$	weft	$\frac{s_b \sin(90° + \theta)}{\sin(\chi - \theta)}$
3	$90° < \chi < \alpha_2$	weft	$\frac{s_b \sin(90° - \theta)}{\sin(180° - \chi + \theta)}$
4	$\alpha_2 \le \chi < 180$	warp	$\frac{s_a \cos\theta}{\cos(180° - \chi)}$

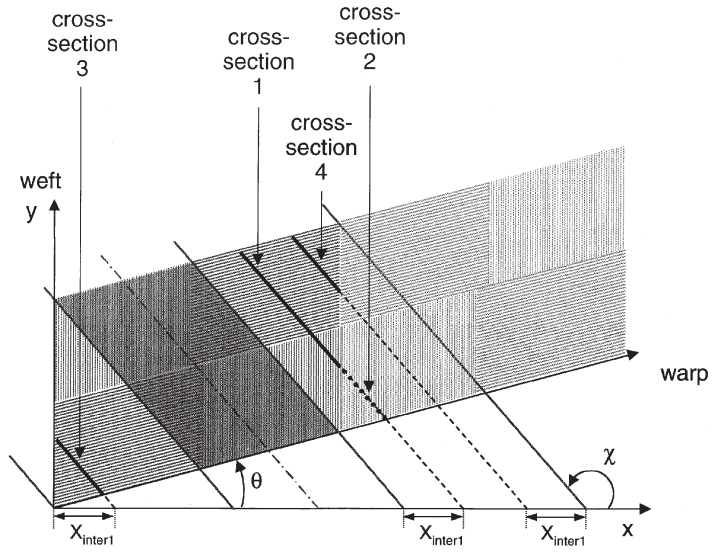

Figure 15. *Cross-section completing process (two representative cells shown). Cross-section 2 is taken from the neighboring representative cell. The shaded area corresponds to the range of complete cross-sections for this particular configuration.*

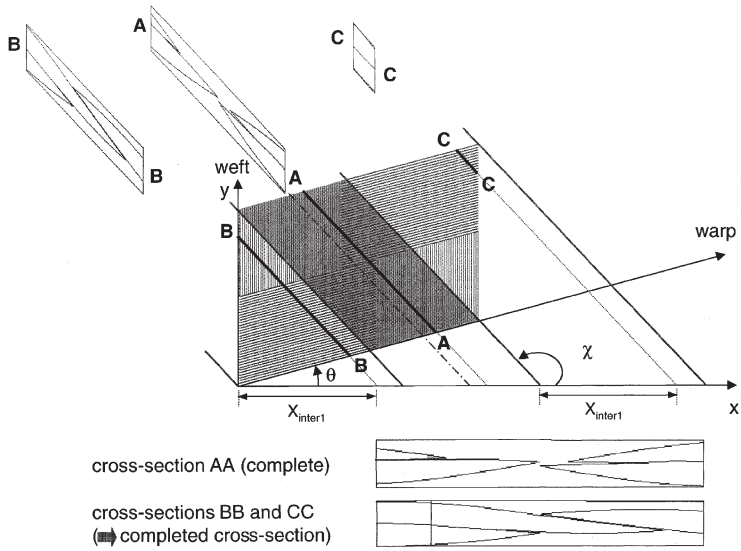

Figure 16. *Examples of cross-section (one representative cell shown): AA, a complete cross-section, and BB and CC, which combine to form a completed cross-section. The shaded area corresponds to the range of complete cross-sections for this particular configuration.*

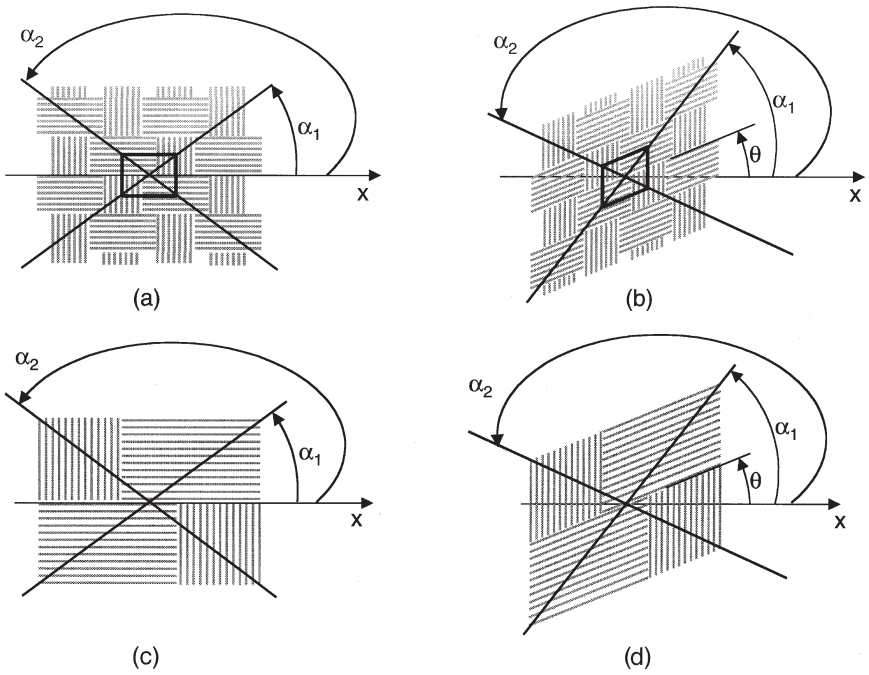

Figure 17. *Critical angles shown on a piece of Knytex 24-5×4 fabric in (a) and (b) and on a representive cell in (c) and (d). The unsheared configuration is shown on the left and a sheared configuration on the right.*

$$\alpha_1 = \tan^{-1}\left(\frac{S_b + S_a \sin\theta}{S_a \cos\theta}\right) \tag{33}$$

$$\alpha_2 = 180 - \tan^{-1}\left(\frac{S_b - S_a \sin\theta}{S_b \cos\theta}\right) \tag{34}$$

Note that the shear angle ranges from 0° (unsheared fabric) to the lock angle, which is about 33 degrees for Knytex 24-5×4.

VERIFICATION OF COMPLETE CHARACTERIZATION

Using these approaches, it was shown that any cross-section that cuts through any piece of plain-weave fabric at any angle χ can be fully reconstituted using complete and completed cross-sections taken from a single representative cell of that fabric at that angle χ. Figure 18 shows the four possible cases described in Table 3 for a fabric sheared by an arbitrary angle θ, with an arbitrary section through

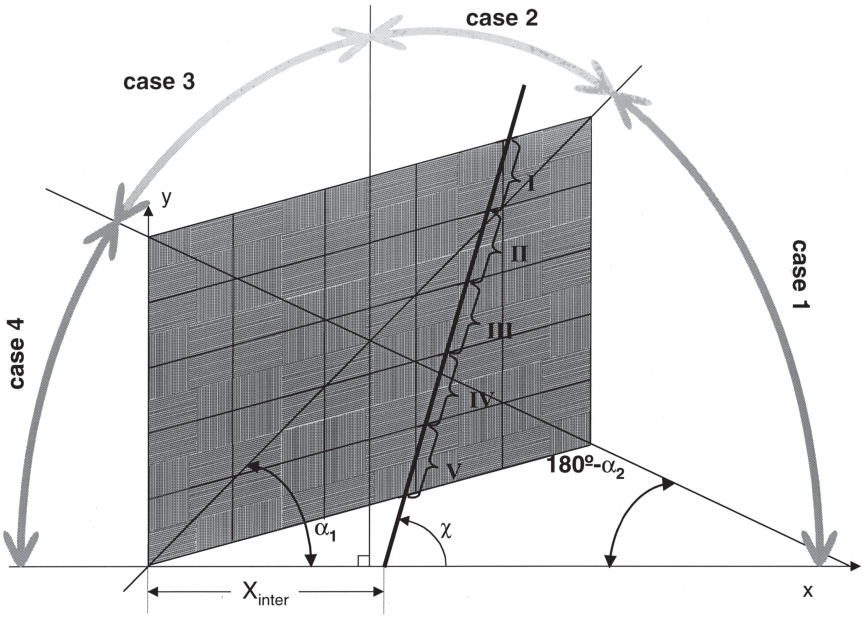

Figure 18. *Top view of a piece of sheared plain-weave fabric made of 25 representative cells showing the 4 case designations (based on the combination of θ and χ as shown in Table 3) and a sample section showing 5 sub-domains: sub-domains II, III, and IV, which are complete cross-section, and sub-domains I and V, which are completed cross-sections.*

the entire piece of fabric taken at an arbitrary cross-section angle χ, through an arbitrary reference point (*x*,*y*). In order to ensure that a minimum but sufficient length has been identified, all complete and completed cross-sections must span two full weft half-tows if the combination of θ and χ corresponds to case 1 or 4 and two full warp half-tows if it corresponds to case 2 or 3. For cases 1 and 4, cross-sections are divided into sub-domains whose limits are representative cell boundaries aligned with the weft. For cases 2 and 3, cross-sections are divided into sub-domains whose limits are representative cell boundaries aligned with the warp. The angle χ shown in Figure 18 is an example of case 2, where a complete or completed cross-section spans two warp half-tows. The sample cross-section shown in Figure 18 has 5 sub-domains: sub-domains II, III, and IV are complete cross-sections, while sub-domains I and V are completed cross-sections since they involve pieces from two different representative cells. For every sub-domain along an arbitrary cross-section, there is a corresponding complete or completed cross-section that can be generated using only one representative cell.

As a way of validating the characterization of the model for the real fabric stud-

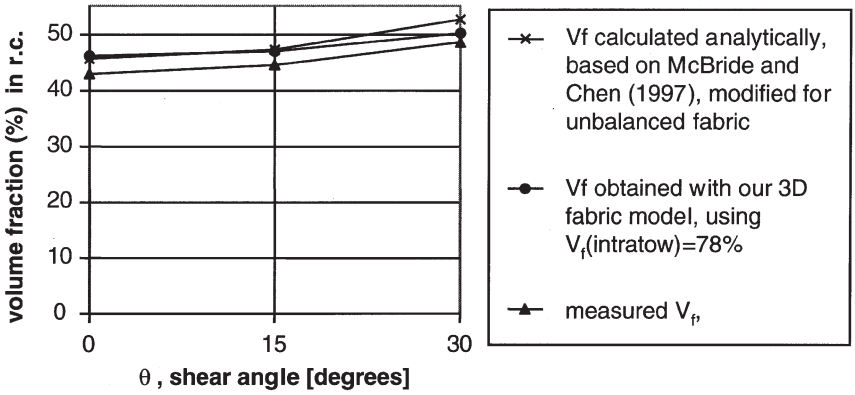

Figure 19. *Volume fraction in a representative cell.*

ied, the volume fraction of the fabric was measured in the laboratory, calculated analytically using the approach of McBride and Chen (1997), and obtained with our 3D fabric model. The results, presented in Figure 19, show good agreement between the experimental data and 3D model presented here, but some discrepancy in the modified McBride and Chen (1997) approach. The modification was performed to adapt the original work to an unbalanced material, but the consequence of the problematic symmetry assumption was not corrected here. The result shows some significant divergence at the high shear angle (~2–3%), motivating the use of a fully 3D model, particularly in areas of high shear.

APPLICATION OF FABRIC MODEL TO MOLD CONDITIONS

Mold Considerations: Stacking and Nesting

Generally, layering of fabrics is poorly controlled and has been identified by other workers as a source of uncertainty in permeation experiments. For example, Jortner (1992) reported that the uncontrolled stacking of plain-weave laminates is "usually oblique" (i.e., neither perfectly nested nor non-nested), but "scattered zones of collimated stacking are also seen." He reported matrix-rich areas containing a larger number of microcracks in regions with "collimated stacking" than in regions with oblique stacking. Yurgartis et al. (1993) reported results on layer nesting distribution based on image analysis. They defined "angle match" as a measure of nesting. Their work, however, was independent of yarn cross-sectional shape. Several authors mentioned nesting as a possible factor, but did not explicitly measure nesting for inclusion in calculations (e.g., Falzon et al., 1996).

Two extreme conditions of nesting are shown in Figure 20, wherein layers are stacked such that tows are aligned [Figure 20(a)], and such that interlayer gaps are minimized [Figure 20(b)]. Sections transverse to the fabric plane are shown in Figure 21. Cases of no nesting [Figures 21(a) and (c)] and perfect nesting [Figures 21(b) and (d)] are shown. Sections in Figures 21(a) and (b) are transverse to the direction in which tow edges abut. Sections in Figures 21(c) and (d) are transverse to the direction in which the tows are spaced, as in the weft direction of the Knytex 24-5×4 fabric shown in Figure 1.

Determination of Thickness Reduction (TR), and Effect on Fabric Permeability

The "nesting" of two or more layers of fabric reduces interlayer gaps and increases the gap between the topmost layer and the mold top. TR, the thickness reduction of the stack, is shown schematically in Figure 22. Maximum nesting and thickness reduction occur when layers are offset by half a representative cell along both the warp and the weft. In order to determine the maximum possible thickness reduction for Knytex 24-5×4, a three-dimensional model of two fabric layers over an area of one representative cell was constructed with our fabric model. The second layer was made up of one quarter of four different representative cells. Figure 23(a) shows four different ways in which two layers can be stacked. For each of the four configurations, cross-sections through the middle of the full representative cell were taken at cross-section angles varying between 0 and 180 degrees at increments of a few degrees, thus "sweeping" the whole range, as shown in Figure

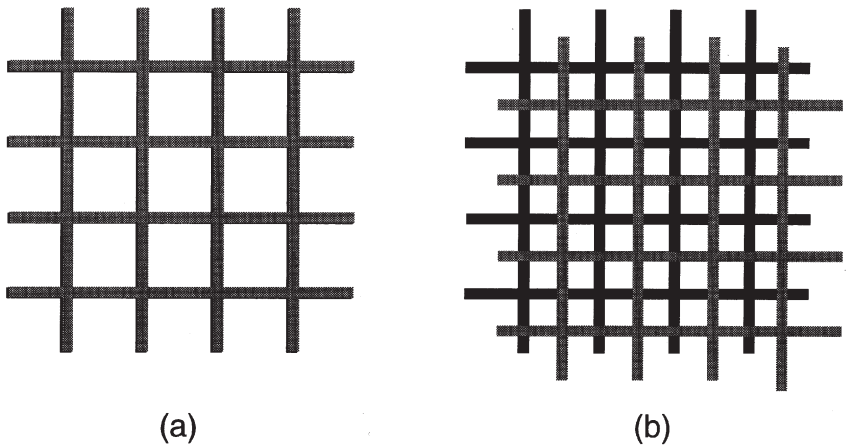

Figure 20. *Top view schematic of two layers of fabric: (a) layers stacked without "nesting," (b) "perfectly nested" layers.*

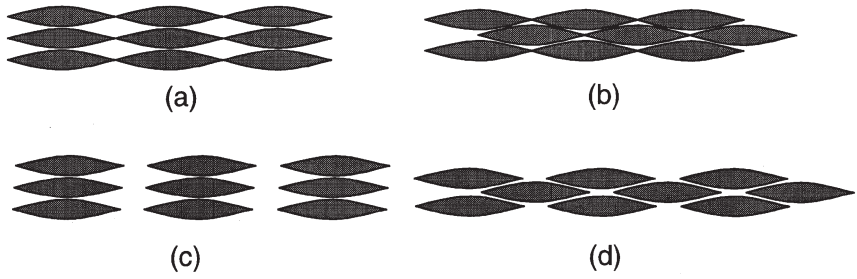

Figure 21. *Two configurations investigated for layer nesting: fabric with tow edges which touch (a and b) and fabric with tow edges which are separated (c and d). The extremes of nesting are shown for each case, including layers with no nesting (a and c) and layers which are "perfectly nested" (b and d).*

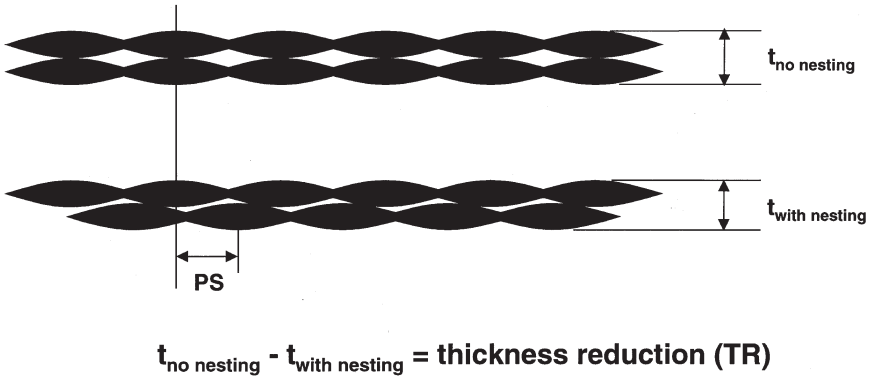

Figure 22. *Cross-sectional schematic of two layers of fabric: (a) layers stacked without "nesting" and (b) "perfectly nested" layers.*

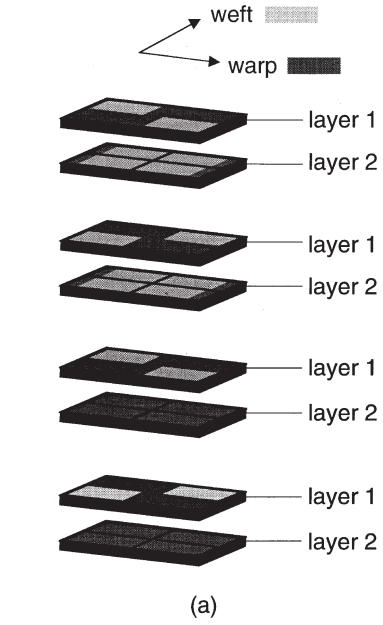

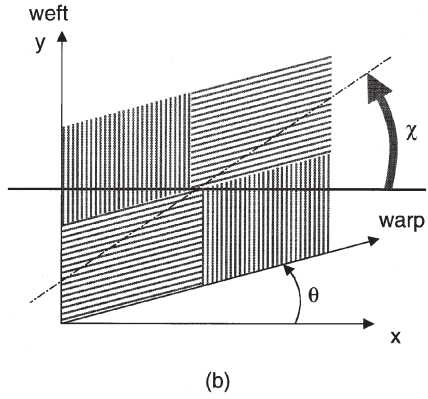

Figure 23. *Determination of possible thickness reduction, shown here for fabric sheared by an angle* θ*. Part (a) shows the 4 possible ways representative cells from two layers offset by* $S_a/2$ *in the* a *direction and* $S_b/2$ *in the* b *direction can be stacked: top face of layer 1 against top face of layer 2, top face of layer 1 against bottom face of layer 2, bottom face of layer 1 against top face of layer 2, and bottom face of layer 1 against bottom face of layer 2. (For the 3D model, only the quarter of interest of each of the 4 representative cells shown for layer 2 was modeled.) The "sweeping" technique by which the maximum possible thickness reduction for a given shear angle was found is shown in (b). For each of the 4 cases shown in (a),* χ *was varied over its entire range of 0° to 180° (a section at* $\chi + 180$ *is the same as the one at* χ*).*

23(b). For every cross-section, the maximum amount by which the distance between the two layers could decrease was determined. An example is shown in Figure 24, where (a) through (d) show the 4 configurations and (e) the configuration offering maximum TR [in this case, configuration (c)], after z translation by TR. Results are shown in Figure 25.

Out of all the possible thickness reductions that were obtained for the different cases, the lowest one was the limiting case and was therefore the maximum possible thickness reduction. This procedure was repeated for the three shear angles considered in this study. The same maximum thickness reduction value of 0.213 mm was obtained for $\theta = 0$, 15, and 30 degrees.

For most of our experiments, 4 layers were placed in a 3.175-mm-thick mold. Since the nominal thickness of a fabric layer is 0.737 mm, the thickness of the 4-layer stack was between 2.31 mm (maximum TR) and 2.95 mm (no nesting). To determine whether significant Poiseuille-type flow was likely occurring between the bottom of the mold top and the upper surface of the top fabric layer, flow experiments with 7 and 8 unsheared fabric layers in a 6.35-mm-thick mold were performed as part of the present study (see Figure 26). The experiments using 8 layers yielded very similar permeabilities to those obtained with 4 unsheared layers in the 3.175-mm-thick mold (as shown in Table 4). When 7 layers were present, Poiseuille flow between the bottom of the mold top and the upper surface of the top fabric layer was obvious, and the flow was one or-

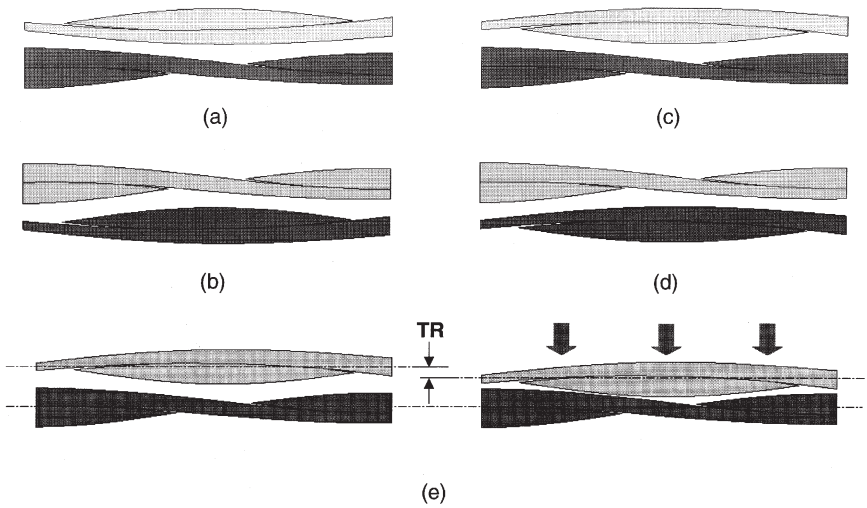

Figure 24. *Cross-sections through 2 layers of fabric. Views (a) through (d) represent cross-sections corresponding to the 4 stacking cases for a particular example ($\theta = 0°$, $\chi = 170°$, $x_{inter} = 0.646$). Fabric section (e) shows nested layers with thickness reduction for case (c).*

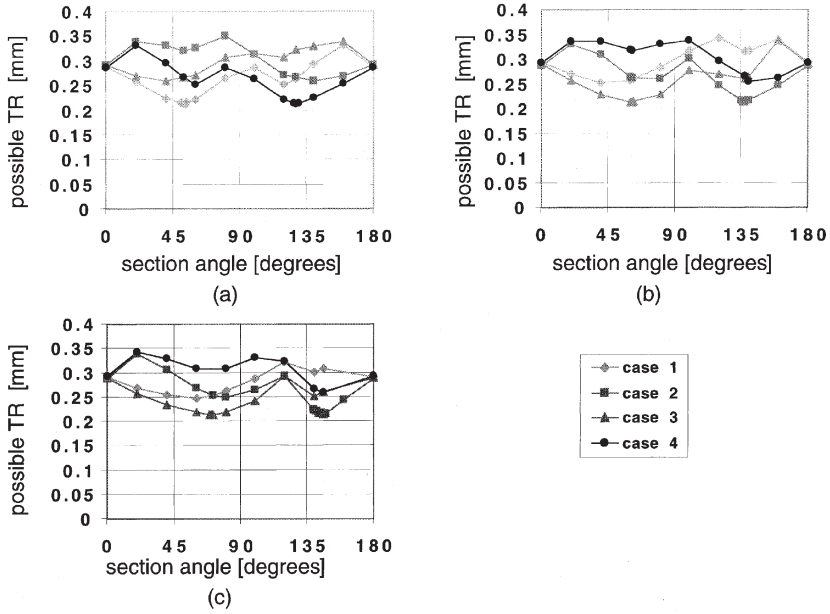

Figure 25. *Possible thickness reduction vs. section angle, shown for the four possible stacking cases of Figure 23, for the following shear angles: (a) θ = 0°, (b) θ = 15°, and (c) θ = 30°.*

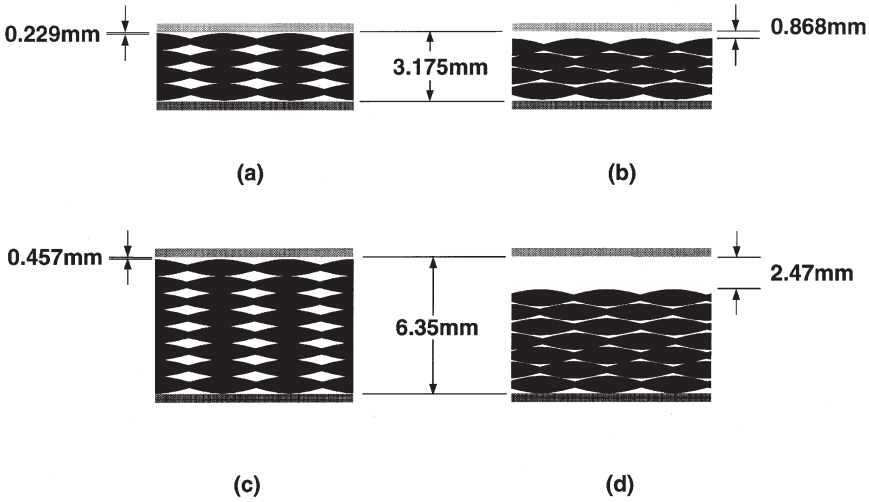

Figure 26. *Schematic of fabric in mold, using experimental dimensions, for (a) 4 layers in 3.175-mm thick mold, ply shift = 0, (b) 4 layers in 3.175-mm thick mold, ply shift = S/2, (c) 8 layers in 6.35-mm thick mold, ply shift = 0, (d) 7 layers in 6.35-mm thick mold, ply shift =S/2.*

Table 4. Experimental permeabilities for 7-layer and 4-layer cases, obtained in the present study on Knytex 24-5×4.

K_1 for 7 layers in 0.635-mm-thick mold (unsat)	4.64×10^{-9} m^2
K_2 for 7 layers in 0.635-mm-thick mold (unsat)	4.29×10^{-9} m^2
K_1 for 4 layers in 0.318-mm-thick mold (unsat)	6.32×10^{-10} m^2
K_2 for 4 layers in 0.318-mm-thick mold (unsat)	5.45×10^{-10} m^2
K_1 for 8 layers in 0.635-mm-thick mold (unsat)	4.98×10^{-10} m^2
K_2 for 8 layers in 0.635-mm-thick mold (unsat)	4.34×10^{-10} m^2

der of magnitude faster than for the case of 4 unsheared layers in the 3.175-mm-thick mold.

DISCUSSION/FUTURE WORK

A fully three-dimensional model for plain-weave fabric was presented. The model can be used for balanced and unbalanced fabric with closed-packing and/or open-packing. We showed that a fully 3D model required greater description than an earlier model by McBride and Chen (1997). Further, an algorithm was developed to describe cross-sections through one or several representative cells at any point and angle. Thus, we were able to examine the microarchitecture of the fabric at different shear angles. Each cross-section shows what the flow actually encounters at that particular point when travelling in a direction normal to the cross-section. Gaps between tows and the effect of nesting on their geometry were of particular interest. Thus, the model developed allows direct simulation of flow in fabric gaps.

The strong effect of nesting was quantified using the newly developed 3D model. With layers of 0.737 mm thickness, the gap between the topmost layer and the mold top increased nearly fourfold (0.229 mm to 0.868 mm) for the 4-layer experiments reported here and in our previous work (Dungan et al., 1999). Gap dimension increased over fivefold (0.457 mm to 2.47 mm) for the 8-layer experiments reported here. Thus, the effect of nesting is clear: the gap flow within the fabric stack, dominant for low-Re flows, is significantly enhanced when materials are not nested, while gaps much greater than layer thicknesses can easily be created between the top of the fabric stack and the mold if many layers are used. These results are used to bound predictions on permeabilities in Part II of this work (Senoguz et al., 2001).

By performing more experiments on permeability for the present study, varying the thickness of the mold cavity and the number of layers in the experiment, we were able to investigate the possible influence of Poiseuille flow on our earlier results. Our conclusions from these observations were that Poiseuille flow occurring

between the bottom of the mold top and the upper surface of the top fabric layer was not significant in our experiments, since gaps arising in the case of maximum nesting, as shown in Figure 26(b), would be comparable in height to those created by using 7, rather than 8, layers in the 6.35-mm-thick mold. Similarly, we concluded that maximum nesting between all layers did not occur in our experiments.

The same maximum thickness reduction value of 0.213 mm was obtained for $\theta = 0$, 15, and 30 degrees. Thus, there appears to be no geometric reason for differences in nesting due to shear. There may, however, be practical reasons that shear induces greater nesting, such as greater interlayer sliding in the presence of shear, which is inhibited when the layers become nested. Our own permeability data, for both saturated and unsaturated cases, shows that permeability first decreases and then increases with increasing shear; nesting may be a contributing effect.

In Part II of this work, our fabric model is used to determine permeabilities based on the geometry of gap between tows. Future work on the fabric model includes modifying the model for different types of fabric (other weaves, braided fabrics, knitted fabrics).

NOMENCLATURE

c	Kozeny constant
$2h$	thickness of a fabric layer
K	permeability
K_1	larger principal permeability
K_2	smaller principal permeability
L_{sect}	length of a complete or completed cross-section
∇P	pressure gradient
PS	ply shift
R	fiber radius
S	length of a fabric representative unit cell
TR	thickness reduction
$\bar{v}$	average fluid velocity
V_f	volume fraction
w	yarn width
x_{inter}	reference point on the x-axis
α_i	critical angles (i = 1,2)
β	half period of sinusoid describing yarn cross-section
η	principal flow angle
θ	shear angle
90-θ	angle between warp and weft
μ	fluid viscosity
χ	cross-section angle

Subscripts

0	value in the unsheared configuration
a	value in the warp direction
b	value in the weft direction
e	refers to sharp corners of a cross-section
m	refers to the midplane of a representative cell
calc	calculated value
exp	experimental value
sat	saturated value
unsat	unsaturated value

Abbreviations

r.c.	representative cell
err	error

ACKNOWLEDGEMENTS

The authors gratefully acknowledge support for this project from the U.S. Army TACOM, General Motors, the NSF SIUCRC on Low Cost, High Speed Polymer Composite Processing, and a National Science Foundation PECASE grant. Support for FDD from a François-Xavier Bagnoud fellowship (Department of Aerospace Engineering, University of Michigan) is also gratefully acknowledged.

REFERENCES

Binétruy, C., B. Hilaire and J. Pabiot. 1998. "Tow Impregnation Model and Void Formation Mechanisms during RTM," *Journal of Composite Materials,* Vol. 32, No. 3, pp. 223–245.

Calhoun, D.R., S. Yalvac, D.G. Wetters, and C.A. Raeck. 1996. "Critical Issues in Model Verification for the Resin Transfer Molding Process," *Polymer Composites,* Vol. 17, No. 1, pp. 11–22.

Dasgupta, A. and R.K. Agarwal. 1992. "Orthotropic Thermal Conductivity of Plain-Weave Fabric Composites Using a Homogenization Technique," *Journal of Composite Materials,* Vol. 26, No. 18, pp. 2736–2758.

Dungan, F.D. 2000. "Investigation of Microscale Flow Phenomena in Determining Permeabilities of Fabrics for Composites," Ph.D. Thesis. University of Michigan.

Dungan, F.D., M.T. Senoguz, A.M. Sastry, and D.A. Faillaci. 1999. "On the Use of Darcy Permeability in Sheared Fabrics," *Journal of Reinforced Plastics and Composites,* Vol. 18, No. 5, pp. 472–484.

Falzon, P.J., I. Herszberg and V.M. Karbhari. 1996. "Effects of Compaction on the Stiffness and Strength of Plain Weave Fabric RTM Composites," *Journal of Composite Materials,* Vol. 30, No. 11, pp. 1210–1247.

HYPERMESH. 1997. *HYPERMESH 2.1 User's Manual.* Troy, MI: Altair Computing, Inc.

Jortner, J. 1992. "Microstructure of Cloth-Reinforced Carbon-Carbon Laminates," *Carbon,* Vol. 30, No. 2, pp. 153–163.

Lai, C.-L. and W.-B. Young. 1997. "Model Resin Permeation of Fiber Reinforcements after Shear Deformation," *Polymer Composites,* Vol. 18, No. 5, pp. 642–648.

Lai, C.-L. and W.B. Young. 1999. "Modeling Fiber Slippage During the Preforming Process," *Polymer Composites,* Vol. 20, No. 4, pp. 594-603.

McBride, T.M. and J. Chen. 1997. "Unit-Cell Geometry in Plain-Weave Fabrics during Shear Deformations," *Composites Science and Technology,* Vol. 57, pp. 345–351.

Peirce, F.T. 1937. "The Geometry of Cloth Structure," *Journal of the Textile Institute,* Vol. 28, pp. T45–T96.

Phelan, F.R. and G. Wise. 1996. "Analysis of Transverse Flow in Aligned Fibrous Porous Media," *Composites Part A,* Vol. 27A, No. 1, pp. 25–34.

Senoguz, M.T., F.D. Dungan, A.M. Sastry, and J.T. Klamo. 2001. "Simulations and Experiments on Low-Pressure Permeation of Fabrics: Part II—Fluid Mechanics," *Journal of Composite Materials*, Vol. 35, No. 14, pp. 1285–1322.

Smith, P., C.D. Rudd, and A.C. Long. 1997. "The Effect of Shear Deformation on the Processing and Mechanical Properties of Aligned Reinforcements," *Composites Science and Technology,* Vol. 57, pp. 327–344.

Tan, P., L. Tong, and G. P. Steven. 1997. "Modelling for Predicting the Mechanical Properties of Textile Composites—A Review," *Composites Part A,* Vol. 28A, pp. 903–922.

Tucker, C.L. and R.B. Dessenberger. 1994. "Governing Equations for Flow and Heat Transfer in Stationary Fiber Beds," Ch. 8 in *Flow and Rheology in Polymer Composites Manufacturing,* S.G. Advani (ed.), Elsevier.

Yurgartis, S.W., K. Morey and J. Jortner. 1993. "Measurement of Yarn Shape and Nesting in Plain-Weave Composites," *Composites Science and Technology,* Vol. 46, pp. 39–50.